Microcavity Laser Oscillating in a Circuit-Based Resonator

Christoph Walther, *et al.*

Science **327**, 1495 (2010);
DOI: 10.1126/science.1183167

Microcavity Laser Oscillating in a Circuit-Based Resonator

Christoph Walther,* Giacomo Scalari, Maria Ines Amanti, Mattias Beck, Jérôme Faist*

Lasers based on microcavities are extremely attractive for their compactness, low power dissipation, and potential for ultrafast modulation speed. We describe an ultrasmall laser based on a subwavelength electronic inductor-capacitor (LC) resonant circuit that allows for extreme confinement of the electric field. This electrically injected laser operates at a frequency of 1.5 terahertz, and the mode volume is strongly subwavelength. The design concept of the LC resonator can be extended from the terahertz range to higher frequencies and also applied to detectors and modulators.

In microcavities, the large electric field generated by vacuum fluctuations enables the observation of quantum optics effects such as the Purcell effect (*1*), which is, in that case, the enhancement of the spontaneous emission by the presence of a strongly confined optical mode (*2*, *3*) or the strong light-matter coupling (*4*). A measure of the confinement is the effective mode volume V_{eff} taken by the energy density of the oscillating electric field. Lasers based on small cavities confined by dielectrics (*5*), such as vertical-cavity surface-emitting lasers (*6*), are limited to V_{eff} values larger than $\sim 2(\lambda/2n_{eff})^3$, where λ is the wavelength, and n_{eff} is the effective refractive index (*7*–*11*). Further reduction of the mode volume beyond these values can only be achieved with the use of metallic cavities. Progress has been made in the use of plasmonic cavities in a waveguide configuration (*12*), with plasmon resonances of nanowires (*13*), or with resonances of nanoparticles (*14*, *15*).

We demonstrate that in the infrared range, the large negative value of the dielectric constant of metals enables the fabrication of lasers using cavities that borrow their concepts from conventional electronics and microwave technology (*16*). These cavities can be seen (Fig. 1A) as consisting of electronic lumped circuit elements: in our case, an inductor-capacitor (LC) resonant circuit (*17*, *18*). Recently, metamaterials based on planar subwavelength lumped circuit resonators were used to design artificial magnetic and electric response in the terahertz range (*19*), and even up to the near-infrared range (*20*). The gain medium [in our implementation, a terahertz quantum cascade (*21*, *22*) active region] is inserted between the plates of the capacitor. Amplification of the electric field in the capacitor by the optical gain medium allows the resonator losses to be overcome, thus leading to self-sustained laser oscillations. This approach is especially well suited for an electrically pumped active region biased by a voltage applied between the metallic capacitor plates. The LC laser enables an effective mode volume much smaller than the cube of the half-wavelength in the material $V_{eff} = 0.12(\lambda/2n_{eff})^3$ and also smaller than has previously been reported for other electrically pumped cavities (*9*, *12*, *23*). Moreover, a further reduction in size is possible by a mere rescaling of the elements. The quality factor Q of the cavities investigated here is limited by ohmic losses. However, it is noteworthy that the radiative losses of resonant LC cavities will decrease as the volume of the cavity decreases (*24*), offering the possibility of a combination of ultrasmall size and very high Q for cavities based on superconductors (*25*).

A scanning electron micrograph image of our device (Fig. 1B) shows that the resonator consists of two half-circular–shaped capacitors connected by a short line acting as an inductor. The geometry that we chose is a compromise between size, losses, and ease of fabrication. To allow electrical pumping of the active medium, we selected a symmetric LC resonator that naturally defines a virtual ground for the resonance frequency in the middle of the inductor that is used for the connection to the bonding pad. A 8-μm-thick active region of a quantum cascade laser having the gain peaked at 1.5 THz (*26*) is inserted between the capacitor plates (Fig. 1C). The fabrication of the LC laser is similar to the fabrication technique used for terahertz double-metal waveguides (*27*). The active material below the bonding pad is electrically isolated from the metal to avoid pumping of the latter. Electromagnetic mode simulations are performed with the use of a commercial software package (*28*). The electric field is found

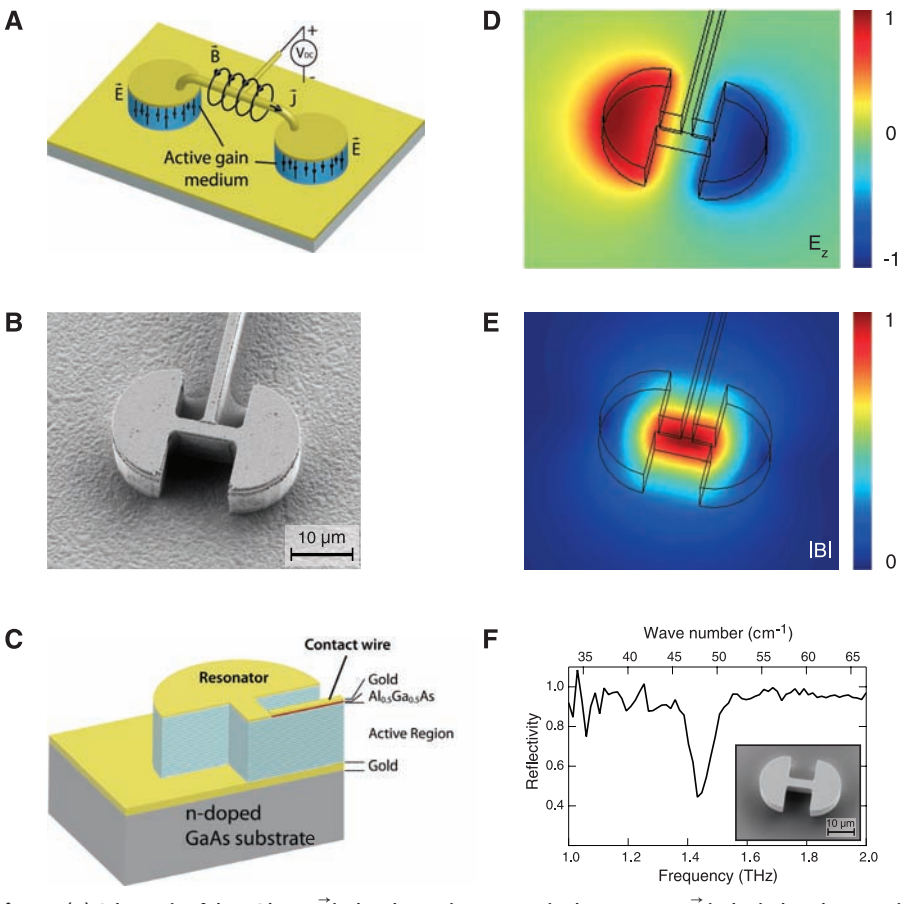

Fig. 1. (**A**) Schematic of the LC laser. $\vec{J}$ is the alternating current in the resonator, $\vec{B}$ is the induced magnetic field, and $\vec{E}$ is the electric field. The active gain medium is biased by the voltage source V_{DC}. (**B**) Scanning electron micrograph picture of the LC laser device. (**C**) Schematic cross section through the device along the symmetry axis. The red layer is undoped $Al_{0.5}Ga_{0.5}As$ and prevents current injection into the active region below the bonding pad. (**D** and **E**) Finite-element simulations of the electromagnetic field in the resonator showing the dominating electric field component E_z and the norm of the magnetic field $|\vec{B}|$. (**F**) Measured reflectivity at 10 K of an array of 400 identical LC resonators, shown in the inset and designed for a frequency of 1.45 THz, without gain medium and without electrical connection.

Institute for Quantum Electronics, ETH Zurich, Wolfgang-Pauli-Strasse 16, 8093 Zurich, Switzerland.

*To whom correspondence should be addressed. E-mail: walther@phys.ethz.ch (C.W.); jerome.faist@phys.ethz.ch (J.F.)

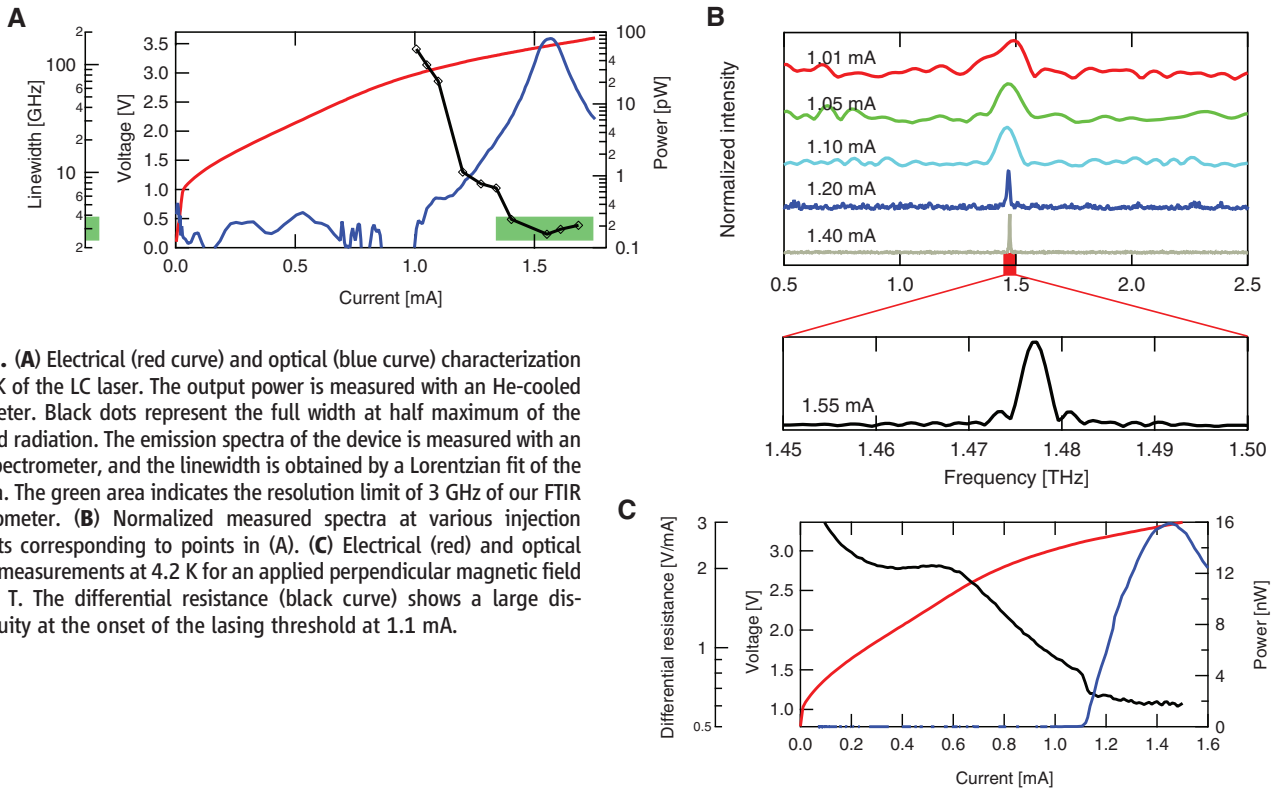

Fig. 2. (**A**) Electrical (red curve) and optical (blue curve) characterization at 10 K of the LC laser. The output power is measured with an He-cooled bolometer. Black dots represent the full width at half maximum of the emitted radiation. The emission spectra of the device is measured with an FTIR spectrometer, and the linewidth is obtained by a Lorentzian fit of the spectra. The green area indicates the resolution limit of 3 GHz of our FTIR spectrometer. (**B**) Normalized measured spectra at various injection currents corresponding to points in (A). (**C**) Electrical (red) and optical (blue) measurements at 4.2 K for an applied perpendicular magnetic field of 2.3 T. The differential resistance (black curve) shows a large discontinuity at the onset of the lasing threshold at 1.1 mA.

to be mainly polarized in the z direction, perpendicular to the capacitors plates, as required by the selection rules of the active gain material. A plot of the electric field component E_z in the resonant mode on a section through the LC resonator at half-gain medium height (Fig. 1D) shows that the electric field is antisymmetric with respect to the axis of symmetry of the structure and is mostly concentrated and uniform under the capacitor plates. The magnetic field (Fig. 1E), on the other hand, is mainly concentrated around the inductor. The laser resonator shown in Fig. 1B is designed for 1.45 THz (λ = 207 μm). We used room-temperature values for the complex refractive index of gold (*29*) to compute a value of the confinement factor of the electric field energy in the active region $\Gamma = 0.85$ and a cold resonator $Q_{ohm} = 53$, mainly caused by ohmic losses in the gold layer. The simulated radiative losses lead to a relatively large radiative $Q_{rad} = 189$, which is in good agreement with the upper limit of 220 given by Wheeler's formula (*24*). The resonator is expected to exhibit a final $Q = 41$, limited by the ohmic losses [supporting online material (SOM) text section S1]. A Purcell factor of 17 is computed, quantifying the enhancement of the spontaneous emission, and mainly limited by the nonradiative transition broadening of the spontaneous emission linewidth. For the validation of the LC resonator concept, we measured the frequency-dependent reflectivity of an array of identical LC resonators without gain medium or electrical connection. The observed absorption resonance of the reflectivity at 1.45 THz with Q = 20 at 10 K (Fig. 1F) is in good agreement with the mode simulation and fits well with a simple calculation based on microwave formulas. An inhomogeneous broadening due to lithographic issues and coupling between resonators explain the lower measured Q of the LC array, compared with the single-resonator Q (SOM text S2).

Fig. 3. Lithographic tuning of the laser frequency by changing the inductor length of the resonator.

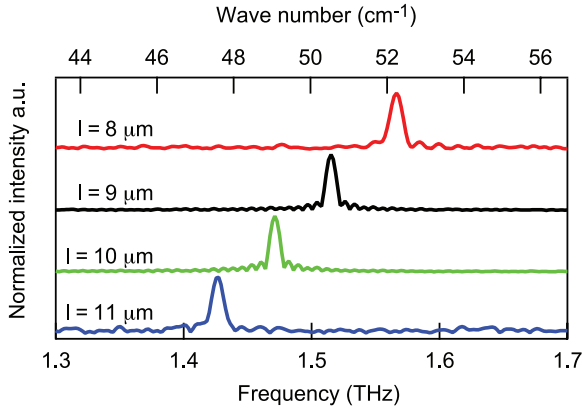

The light and voltage versus current characteristics of a LC laser operated at 10 K show a strong increase in the optical power observed at a current of ~1.20 mA, as the voltage reaches the value corresponding to the alignment of the structure, with a maximum detected peak power of ~80 pW reached at 1.55 mA (Fig. 2A). To characterize the nature of the emission, we performed a measurement of the device spectrum as a function of increasing current. The spectra in Fig. 2B show a single emission line peaking at a frequency of 1.477 THz, close to the value expected by simulation of 1.45 THz. At currents between 1.01 and 1.10 mA, corresponding to the lowest detectable optical signal, the linewidth corresponds to Q = 11 to 21, which is lower than the value computed for the cold cavity. This discrepancy is attributed to two different factors: First, during the alignment regime of the quantum structure near 1 mA, the active-region losses may be higher than at the threshold (*30*). Second, as the transition occurs between two states with a clear spatial separation, the gain curve exhibits a strong Stark shift with the applied bias. At low biases, the gain peaks at 1.3 THz and is therefore clearly detuned from the cavity resonance, which acts as a filter to further broaden the emission spectrum. The observation of electroluminescence at such low current and frequency points toward a large value of the Purcell factor. As the current is increased, the linewidth decreases steeply and falls below the resolution limit of our Fourier

transform infrared (FTIR) spectrometer, corresponding to a linewidth of ~3 GHz at a current of 1.4 mA and a detected power of ~7 pW. As the current is increased beyond this value, any further narrowing of the transition is hidden behind the limitation of our measurement system. The plot of the linewidth versus injected current combined with the super-exponential increase of the optical power in Fig. 2A strongly suggests that the device is reaching the laser threshold regime near to 1.5 mA. However, the gain in our structure is not sufficient to operate the device clearly in the regime above the lasing threshold.

To access the operation in this regime, we have enhanced the gain of the active medium by immersing the device in a strong magnetic field perpendicular to the quantum wells plane. The magnetic field breaks the in-plane parabolic energy dispersion of the electronic subbands and leads to the formation of discrete Landau levels, allowing the creation of quasi–zero-dimensional states. The spacing of the Landau levels is equal to the cyclotron energy $E_c = \hbar eB/m^*$, where $\hbar$ is Planck's constant divided by 2π, B is the magnetic field, e is the electron charge, and m^* is the effective mass of the electron. By varying the relative ratio between the cyclotron energy and sub-band energy spacing, the electron dynamics and the subsequent lasing properties of a terahertz quantum cascade laser are strongly affected (*31*). The optical characteristics of the LC laser in a magnetic field of 2.3 T (Fig. 2C) show that, above the threshold, the power increases linearly with the current up to 16 nW until the electrical roll-over is reached. The onset of lasing is accompanied by an abrupt decrease of the differential resistance and is a clear demonstration of the lasing threshold (*32*). By measuring the threshold current of a control laser with a conventional metal-metal waveguide, we estimate an enhancement of the gain due to the magnetic field by 5 to 10% at 2.3 T.

A number of resonant cavities have been fabricated, continuously modifying the value of the inductor. As expected, the emission spectra (Fig. 3) shift correspondingly between 1.43 and 1.57 THz. The spectra of the devices operating in the edge of the gain curve are barely reaching the threshold regime because they are strongly detuned from the maximum of the gain curve.

Our ultrasmall, electrically injected laser based on a resonator combines elements from microwave electronics with a gain medium. The strong confinement achievable with resonant LC cavities is of great interest for both applications and quantum optics studies. Our results can be seen as implementing gain in one cell of a LC-based metamaterial (*33*). Because of its monomode output, low dissipation, and tunability, such a source could be integrated with hot-electron bolometers to create arrays of highly sensitive heterodyne receptors for demanding applications such as radio-astronomy (*34*). The strong coupling that is achieved in such resonators could also lead to interesting applications, not only for optical sources, but also for detectors and modulators, as the latter devices do not require very high Q factors and would benefit greatly from the reduction of the mode volume brought by this resonator. V_{eff} can be reduced almost at will, as long as the reduction in the capacitance can be compensated by an increase of the inductance to keep the product constant. An attractive feature of the LC resonator is the spatial separation of the electric and magnetic fields, simultaneously allowing extremely high confinement of the electric field and an efficient out-coupling to the environment by the magnetic field. An LC resonator with a bent inductor could act as a magnetic loop antenna, which is efficiently coupled to both the vacuum and the matter, such as a quantum dot (SOM text S3). The design concept of the LC resonator can be extended from the terahertz range to near-infrared frequencies (SOM text S4).

References and Notes

1. E. M. Purcell, *Phys. Rev.* **69**, 681 (1946).
2. J. Gérard *et al.*, *Phys. Rev. Lett.* **81**, 1110 (1998).
3. S. Ogawa, M. Imada, S. Yoshimoto, M. Okano, S. Noda, *Science* **305**, 227 (2004); published online 3 June 2004 (10.1126/science.1097968).
4. C. Weisbuch, M. Nishioka, A. Ishikawa, Y. Arakawa, *Phys. Rev. Lett.* **69**, 3314 (1992).
5. K. J. Vahala, *Nature* **424**, 839 (2003).
6. F. Koyama, *Lightwave Technol.* **24**, 4502 (2006).
7. R. Coccioli, M. Boroditsky, K. W. Kim, Y. Rahmat-Samii, E. Yablonovitch, *IEE Proc. Optoelectron.* **145**, 391 (1998).
8. O. Painter *et al.*, *Science* **284**, 1819 (1999).
9. H.-G. Park *et al.*, *Science* **305**, 1444 (2004).
10. J. Scheuer, W. Green, G. DeRose, A. Yariv, *Appl. Phys. Lett.* **86**, 251101 (2005).
11. K. Nozaki, T. Baba, *Appl. Phys. Lett.* **88**, 211101 (2006).
12. M. Hill *et al.*, *Nat. Photonics* **1**, 589 (2007).
13. R. F. Oulton *et al.*, *Nature* **461**, 629 (2009).
14. S. Kühn, U. Håkanson, L. Rogobete, V. Sandoghdar, *Phys. Rev. Lett.* **97**, 017402 (2006).
15. M. A. Noginov *et al.*, *Nature* **460**, 1110 (2009).
16. J. Slater, *Rev. Mod. Phys.* **18**, 441 (1946).
17. The lumped element circuit approach was proposed at optical frequencies (*18*).
18. N. Engheta, *Science* **317**, 1698 (2007).
19. T. J. Yen *et al.*, *Science* **303**, 1494 (2004).
20. S. Linden *et al.*, *Science* **306**, 1351 (2004).
21. J. Faist *et al.*, *Science* **264**, 553 (1994).
22. R. Köhler *et al.*, *Nature* **417**, 156 (2002).
23. Y. Chassagneux *et al.*, *Appl. Phys. Lett.* **90**, 091113 (2007).
24. H. Wheeler, *IRE Trans. Antennas Propag.* **35**, 1479 (1947).
25. A. Wallraff *et al.*, *Nature* **431**, 162 (2004).
26. C. Walther *et al.*, *Appl. Phys. Lett.* **91**, 131122 (2007).
27. B. Williams, S. Kumar, Q. Hu, J. Reno, *Opt. Express* **13**, 3331 (2005).
28. Multiphysics Modeling and Simulation Software (COMSOL) was used for our simulations (www.comsol.com).
29. M. Ordal, R. Bell, R. Alexander Jr., L. Long, M. Querry, *Appl. Opt.* **26**, 744 (1987).
30. G. Scalari *et al.*, *Laser and Photonics Rev.* **3**, 45 (2009).
31. G. Scalari *et al.*, *Phys. Rev. Lett.* **93**, 237403 (2004).
32. C. Sirtori *et al.*, *IEEE J. Quantum Electron.* **34**, 1722 (1998).
33. M. Wegener *et al.*, *Opt. Express* **16**, 19785 (2008).
34. J. Gao *et al.*, *Appl. Phys. Lett.* **86**, 244104 (2005).

35. We thank the Swiss National Science Foundation and the National Center of Competence in Research "Quantum Photonics" for support and L. Nevou for key contributions to the reflectivity measurement. This work was partly carried out in the Center for Micro- and Nanotechnology (FIRST) at ETH Zurich. J.F. would like to acknowledge fruitful discussions with E. Yablonovitch and A. Imamoglu.

Supporting Online Material

www.sciencemag.org/cgi/content/full/327/5972/1495/DC1
Materials and Methods
SOM Text
Figs. S1 to S4
References

12 October 2009; accepted 11 January 2010
10.1126/science.1183167

The Climatic Signature of Incised River Meanders

Colin P. Stark,[1]* Jonathan R. Barbour,[1] Yuichi S. Hayakawa,[2] Tsuyoshi Hattanji,[3] Niels Hovius,[4] Hongey Chen,[5] Ching-Weei Lin,[6] Ming-Jame Horng,[7] Kai-Qin Xu,[8,9] Yukitoshi Fukahata[10]

Climate controls landscape evolution, but quantitative signatures of climatic drivers have yet to be found in topography on a broad scale. Here we describe how a topographic signature of typhoon rainfall is recorded in the meandering of incising mountain rivers in the western North Pacific. Spatially averaged river sinuosity generated from digital elevation data peaks in the typhoon-dominated subtropics, where extreme rainfall and flood events are common, and decreases toward the equatorial tropics and mid-latitudes, where such extremes are rare. Once climatic trends are removed, the primary control on sinuosity is rock weakness. Our results indicate that the weakness of bedrock channel walls and their weakening by heavy rainfall together modulate rates of meander propagation and sinuosity development in incising rivers.

In humid, rapidly eroding (*1*) montane environments such as the Cascades (*2*), Japan (*3*), and Taiwan (*4*), lateral erosion along the banks and walls of bedrock-floored river channels (*5*–*13*) can be as important a process as vertical incision. Rates of lateral erosion can exceed down-cutting rates by over 10 times as a bedrock channel widens (*11*, *12*) or meanders (*5*–*10*, *13*, *14*). With time, such horizontal cutting is known to generate sinuous channels (*5*–*10*, *13*–*20*), very broad channels (*8*, *9*), bedrock-floored cut (strath) terraces (*2*, *5*, *6*, *13*, *21*), asymmetric valleys (*7*, *17*–*19*), and even meander cut-off loops (*8*–*10*, *13*, *15*–*20*). In particular, field observations (*8*–*10*) and theoretical considerations (*22*, *23*) indicate that the majority of the meanders and high sinuosities seen in such bedrock rivers are actively generated by erosive lateral chan-